Serb. Astron. J. № 211 (2025), 9 - 26
DOI: https://doi.org/10.2298/SAJ2511009K

UDC 524.722.7
Original scientific paper

NEW ASKAP RADIO-CONTINUUM SURVEYS OF THE SMALL MAGELLANIC CLOUD

O. K. Khattab[1], M. D. Filipović[1], Z. J. Smeaton[1], R. Z. E. Alsaberi[2,1], E. J. Crawford[1], D. Leahy[3], S. Dai[4,1] and N. Rajabpour[1]

[1] *Western Sydney University, Locked Bag 1797, Penrith South DC, NSW 2751, Australia*
E–mail: *22197951@student.westernsydney.edu.au*

[2] *Faculty of Engineering, Gifu University, 1-1 Yanagido, Gifu 501-1193, Japan*

[3] *Department of Physics and Astronomy, University of Calgary, Calgary, Alberta, T2N IN4, Canada*

[4] *Australian Telescope National Facility, CSIRO, Space and Astronomy, P.O. Box 76, Epping, NSW 1710, Australia*

(Received: August 5, 2025; Accepted: October 28, 2025)

SUMMARY: We present two new radio-continuum images from the Australian Square Kilometre Array Pathfinder (ASKAP) POlarisation Sky Survey of the Universe's Magnetism (POSSUM) survey in the direction of the Small Magellanic Cloud (SMC). The two new source lists produced from these images contain 36,571 radio continuum sources observed at 944 MHz and 15,227 sources at 1367 MHz, with beam sizes of $14\farcs5\times12\farcs2$ and $8\farcs7\times8\farcs2$, respectively. We used the Aegean software to create these point source catalogues, and together with the previously published Meer-Karoo Array Telescope (MeerKAT) point source catalogue, we estimated spectral indices for the whole population of radio point sources in common. By cross-matching our ASKAP catalogues with the MeerKAT catalogue, we found 21,442 and 12,654 point sources in common for 944 MHz and 1367 MHz, respectively, within a $2''$ region. This point source catalogue will help to further our knowledge of the SMC and highlights the power of the new generation of telescopes such as ASKAP in studying different galactic populations.

Key words. Radio continuum: general – Surveys – Catalogs – Galaxies: individual: Small Magellanic Cloud – Techniques: image processing

1. INTRODUCTION

Over the past 50 years, advances in radio astronomy have improved our knowledge and understanding of the Small Magellanic Cloud (SMC), a dwarf galaxy orbiting the Milky Way. The SMC is located at a distance of 62.44 ± 0.47 kpc, and has a considerable depth along our line of sight of up to 7 kpc (Hilditch et al. 2005). Recent radio continuum surveys have been conducted at different frequencies, including radio surveys by telescopes such as Meer-Karoo Array Telescope (MeerKAT) (Cotton et al. 2024), the Australian Square Kilometre Array Pathfinder (ASKAP) (Joseph et al. 2019) and the Murchison Widefield Array (MWA) (For et al. 2018). These allow for analysis into how the interstellar medium (ISM) evolves, as well as shedding light on the properties and movements of sources such as supernova remnants (SNRs), planetary nebulae (PNe), young stellar objects (YSOs), and HII regions (Filipović and Tothill 2021).

The first published radio source catalogue of the SMC was released in the 1970s by Clarke (1976), Filipovic et al. (1996), which initiated a series of comprehensive radio astronomy studies. There have

been several surveys conducted since then (McGee et al. 1976, Wright and Otrupcek 1990, Filipovic et al. 1997, Turtle et al. 1998, Filipovic et al. 1998, Filipović et al. 2002, Payne et al. 2004, Filipović et al. 2005, Reid et al. 2006, Payne et al. 2007, Wong et al. 2011a, Crawford et al. 2011, Wong et al. 2011b, 2012a,b, For et al. 2018, Dempsey et al. 2022, Pingel et al. 2022, Murray et al. 2024, Cotton et al. 2024), which have gradually increased our knowledge of the dynamics and structure of the SMC.

These surveys have provided catalogues of SNRs, helping to identify their interactions with the surrounding interstellar medium and refine their distribution across the SMC (Filipović et al. 2005, Payne et al. 2007, Matsuura et al. 2022). Furthermore, the identification and classification of PNe have improved our understanding of their evolution and chemical composition in the context of a dwarf galaxy (Filipovic et al. 1996, 1997, Payne et al. 2004, Asher et al. 2024).

Recent radio-continuum surveys using new-generation interferometers such as ASKAP, MeerKAT, and MWA have revolutionised our ability to study numerous Galactic and extragalactic radio sources and populations. These include discoveries and analyses of several objects, including Galactic and Magellanic Cloud (MC) SNRs (Kothes et al. 2017, Filipović et al. 2023, Burger-Scheidlin et al. 2024, Khabibullin et al. 2023, Smeaton et al. 2024b, Ball et al. 2025, Filipovic et al. 2025, Smeaton et al. 2025) and SNR candidates (Lazarević et al. 2024b, Smeaton et al. 2024a), as well as the discovery of the first intergalactic SNR J0624−6948 (Filipović et al. 2022, Sasaki et al. 2025), and the study of interesting Galactic and extragalactic sources such as reflection nebulae (RNe) (Bradley et al. 2025b), Wolf-Rayet nebulae (Bradley et al. 2025a), pulsar wind nebulae (PWNe) (Lazarević et al. 2024a, Ahmad et al. 2025), active galactic nuclei (AGN) (Velović et al. 2022), and Odd Radio Circles (ORCs) (Norris et al. 2021, Koribalski et al. 2021, Gupta et al. 2022, Norris et al. 2022). These surveys have also advanced our understanding of the evolution of AGN, and star formation processes in low-metallicity environments (Hotan et al. 2021, Urquhart et al. 2022, Cotton et al. 2024). These large-area, high-sensitivity surveys allow for statistical characterisation of compact and extended sources across a range of physical scales, providing insights into the life cycles of galaxies, the role of magnetic fields, and the interaction between massive stars and the ISM (Caleb et al. 2022).

The radio-continuum catalogue of the SMC presented by Joseph et al. (2019) was based on ASKAP early science data taken at 1320 MHz as part of the EMU pilot survey. While the survey was a significant step forward, the dataset was limited by early beam calibration models, reduced uv-coverage, and preliminary imaging and source extraction pipelines. As a result, the positional and flux accuracy, as well as the catalogue completeness, were subject to systematic limitations (Hotan et al. 2021).

This paper presents a new ASKAP radio-continuum survey and its corresponding catalogue. We carry out a comparative analysis with the recently published MeerKAT survey of the SMC by Cotton et al. (2024), leveraging the extensive dataset to validate and assess the quality of our results.

In contrast, the new catalogue presented in this paper is based on ASKAP observations at 944 MHz and 1367 MHz, using the latest imaging and calibration techniques from the ASKAPSoft pipeline (Guzman et al. 2019). The data benefit from improved primary beam models, better dynamic range, and deeper integrations. This catalogue represents an improvement over the earlier work of Joseph et al. (2019), offering enhanced positional accuracy and more reliable flux measurements.

The structure of this paper is as follows: Section 2 describes ASKAP's observations, data, and processing. Section 3 describes ASKAP's point source catalogue generating methodology. Section 4 presents the results of the comparison between the ASKAP and MeerKAT catalogues. Section 5 discusses these results, and Section 6 provides the main conclusions.

2. DATA, OBSERVATION AND PROCESSING

In this section, we present the data and images obtained with ASKAP at 944 and 1367 MHz (McConnell et al. 2016, Hopkins et al. 2025).

The ASKAP Pilot Survey for the POSSUM project code for both surveys is AS103[1] (Gaensler et al. 2025). Observations were conducted on 2022-08-07 and 2022-09-18 using the ASKAP array. The data correspond with scheduling blocks SB43237 (`tilePOSSUM_0101-72`) and SB44127 (`tilePOSSUM_0101-72A`). Observations were made at central frequencies of 944 MHz and 1367 MHz, with corresponding bandwidths of 288 MHz. The beam sizes for the corresponding images are $14\farcs5 \times 12\farcs2$ and $8\farcs7 \times 8\farcs2$, respectively. The average background noise for the images are 26 μJy beam^{-1} and 28 μJy beam^{-1}, respectively (see Table 1).

The data is accessible through the Commonwealth Scientific and Industrial Research Organisation (CSIRO) ASKAP Science Data Archive (CASDA)[2] (Chapman 2015, Chapman et al. 2017, Huynh et al. 2020).

The data reduction was performed with ASKAPSOFT v1.7.1, using the ASKAP pipeline v1.9.5 for the 944 MHz and v1.9.7 for the 1367 MHz, which offers reliable calibration and imaging processes by utilising multi-frequency synthesis imaging and multi-scale cleaning methods (Guzman et al. 2019).

[1] `http://hdl.handle.net/102.100.100/326207?index=1`

[2] `https://data.csiro.au/domain/casda`

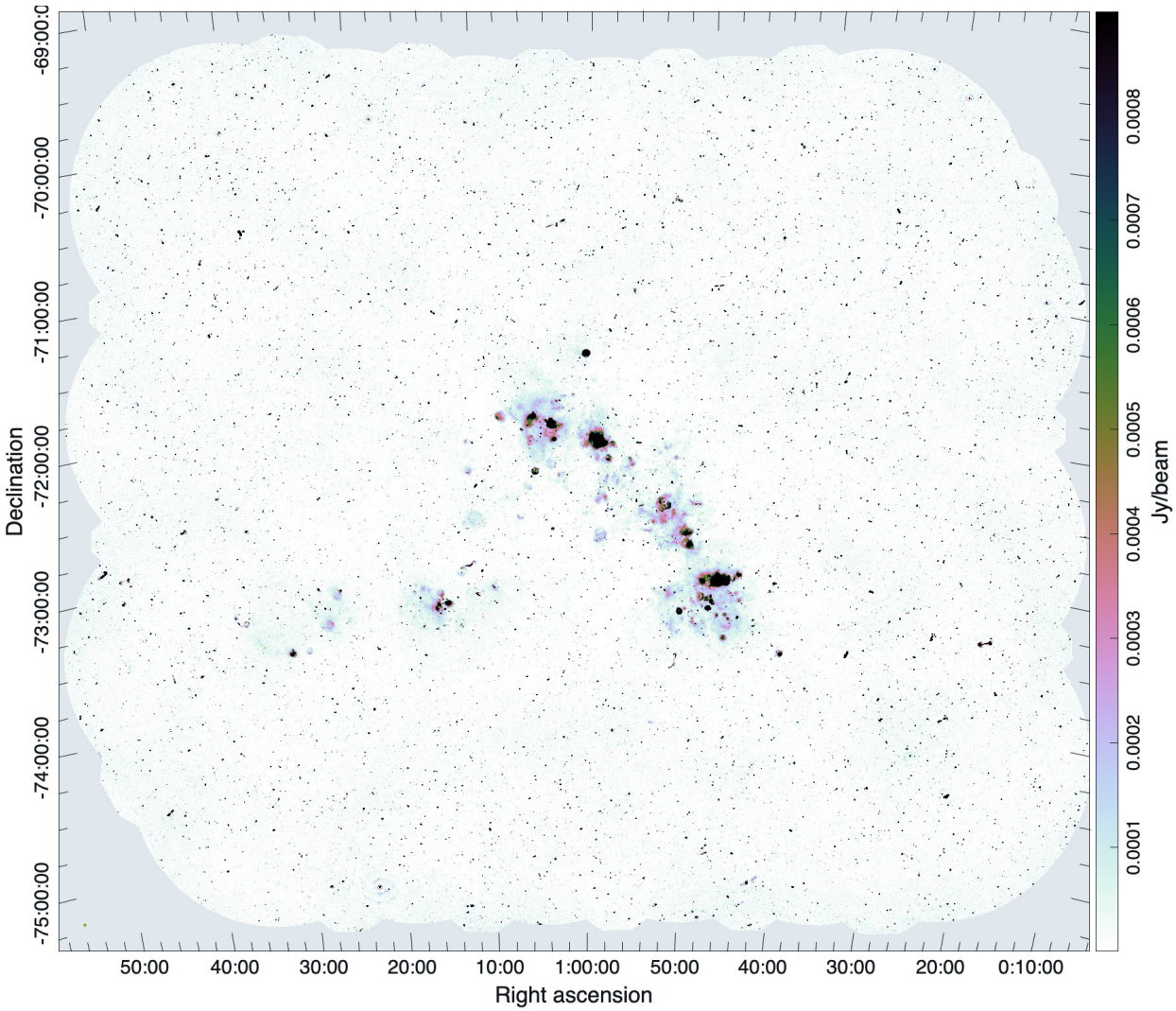

Fig. 1: ASKAP image of the SMC at 944 MHz. The beam size is $14\farcs5 \times 12\farcs2$ and the linearly scaled colour bar represents the image scale intensity range. The background noise level in the image is 26 μJy beam^{-1}. Coordinates are in the epoch J2000.

We show the full ASKAP tiles of the SMC field at the frequencies of 944 MHz (Fig. 1) and 1367 MHz (Fig. 2) using the cubehelix colour scheme (Green 2011). A summary of the ASKAP observations is given in Table 1.

3. POINT SOURCE CATALOGUE GENERATION METHODOLOGY

This section presents the systematic method undertaken to generate the point source catalogue that we adopt in our analysis. This process was optimised to achieve a maximum degree of reliability, completeness, and consistency across the entire observed field. We present the step-by-step data processing and source detection steps, from first source detection to post-processing filters and verification, employed to calibrate the source catalogue and to reduce noise caused by artifacts, extended sources, and noise-limited regions. This process employs automated source-finding programs together with statistically warranted quality assessment criteria and final visual checking, in compliance with best practices in current broad field radio-continuum surveys.

Step 1: Initial source detection and catalogue Generation

The source finding program AEGEAN[3] (Hancock et al. 2012, 2018) was employed to generate initial source lists from the ASKAP images at a 3-sigma detection threshold. These images, which exhibit varying noise levels due to the presence of multiple beams and bright source artifacts, were first processed using

[3] https://github.com/PaulHancock/Aegean

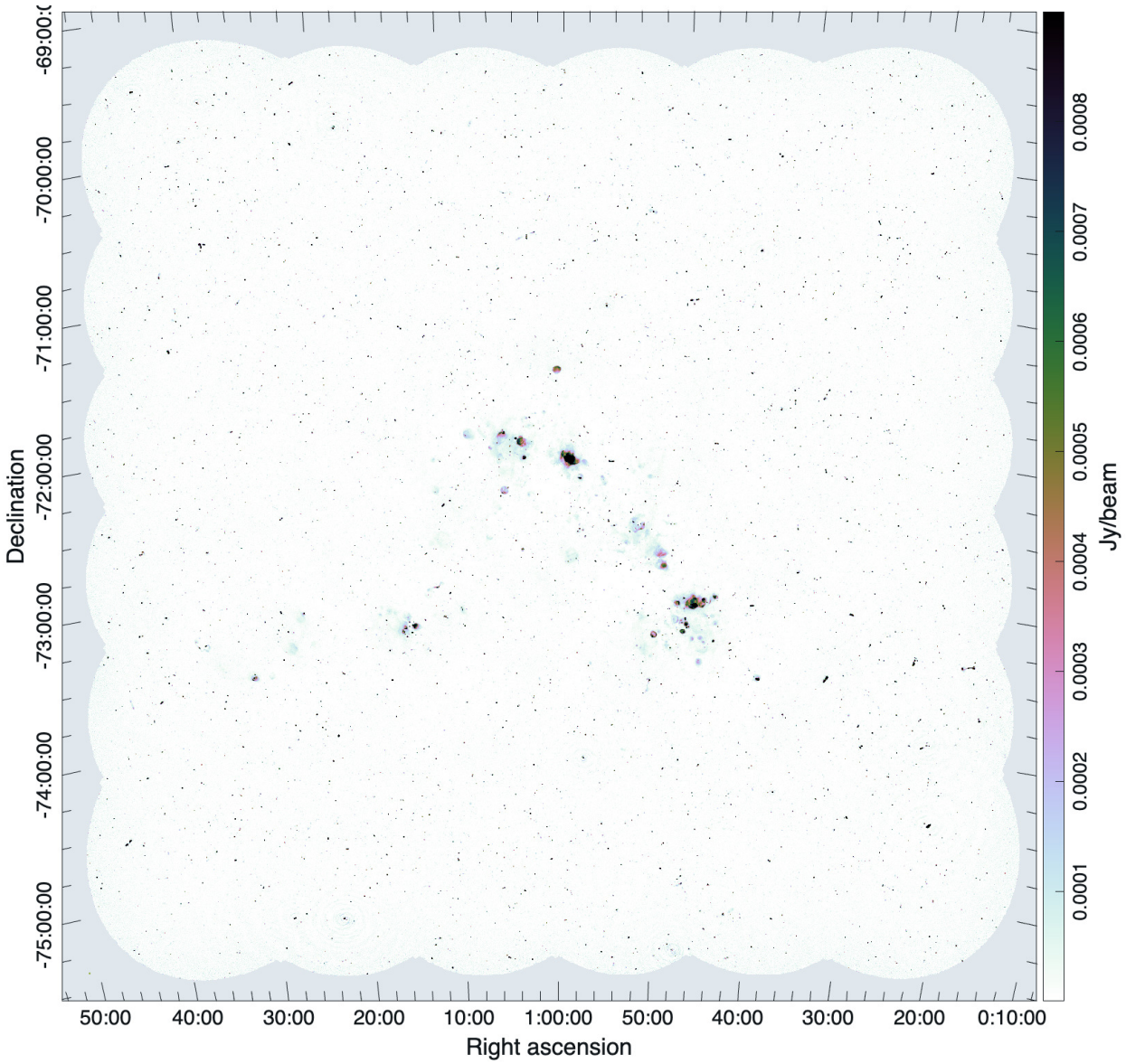

Fig. 2: ASKAP image of the SMC at 1367 MHz. The beam size is $8\farcs7 \times 8\farcs2$ and the linearly scaled colour bar represents the image scale intensity range. The background noise level in the image is 28 μJy beam^{-1}. Coordinates are in the epoch J2000.

Table 1: Summary of ASKAP data and observations.

Frequency (MHZ)	**944 MHz**	**1367 MHz**
Project Code	AS103	
Bandwidth (MHz)	288	
Stokes Parameter	STOKES I	
Observation Date	2022-08-07	2022-09-18
Scheduling Block (SBID)	SB43237	SB44127
Beam Size ($''\times''$)	14.5 × 12.2	8.7 × 8.2
RMS (μJy beam^{-1})	26	30

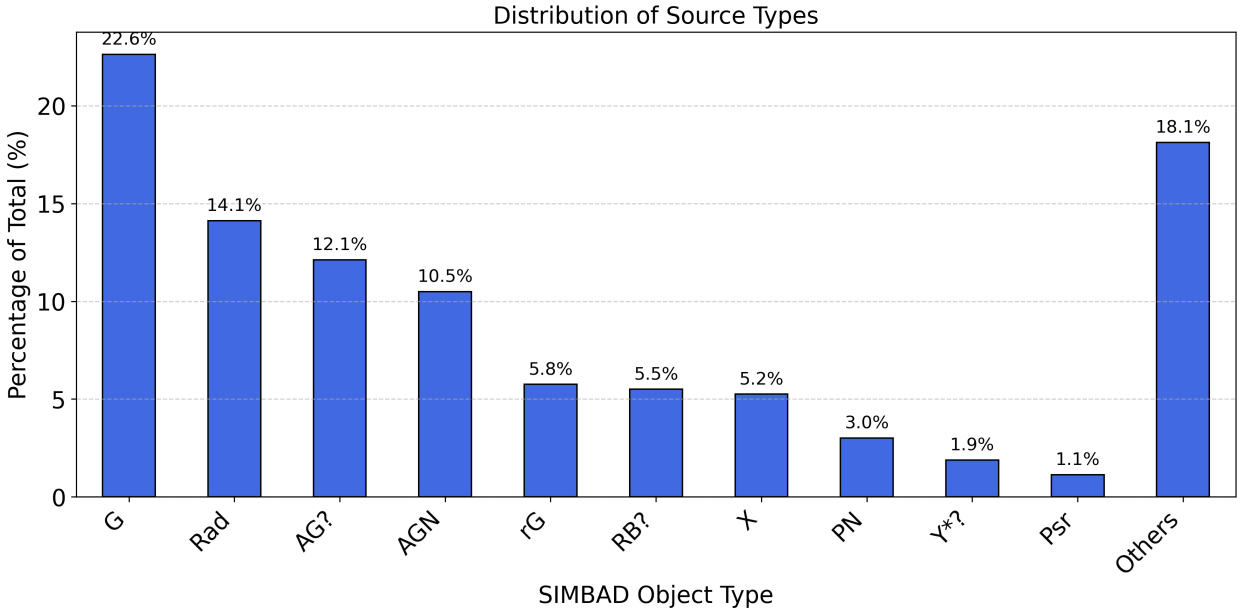

Fig. 3: Distribution of SIMBAD object types from cross-matched sources. G = galaxy; Rad = radio source; AG? = possible active galaxy; AGN = active galactic nucleus; rG = radio galaxy; RB? = possible radio burst source; X = X-ray source; PN = planetary nebula; Y*? = possible young stellar object; Psr = pulsar; Others = rare types.

the Background and Noise Estimator (BANE)[4] routine. BANE generates Root Mean Squared (RMS) background noise maps using a sliding box-car and sigma-clipping algorithm (Hancock et al. 2018). The initial catalogue included all sources detected at the 3-sigma level with default parameters.

Step 2: Masking Sources Based on FLAGS and SOURCES

We excluded sources with `FLAGS` not equal to 0 or `SOURCES` less than 1, following recommendations in the AEGEAN documentation[5]. According to the documentation, non-zero `FLAGS` indicate unreliable fits, while a source count (`SOURCES`) below 1 suggests inadequate detection quality. This step was crucial for ensuring that only well-fit, reliable sources were retained in the final catalogue.

Step 3: Axis Ratio Masking

To exclude extended or poorly resolved sources, we masked sources based on their major and minor axis ratios. The major axis ratio (R_a) and minor axis ratio (R_b) were calculated as follows:

$$R_a = \frac{a}{\mathrm{psf}_a}, \quad R_b = \frac{b}{\mathrm{psf}_b},$$

where a and b are the source's measured major and minor axes, and psf_a and psf_b are the corresponding beam's major and minor axes. A perfect point source should have an angular size equal to the beam size, meaning $R_a = 1$ and $R_b = 1$. Any source with an angular size larger than the beam is considered resolved, while those smaller than the beam are unresolved and handled separately using the peak flux density (S_{peak}) instead of the integrated flux density (S_{int}).

To retain compact sources, we excluded all sources with $R_a > 1.2$ or $R_b > 1.2$, corresponding to 20% larger than the beam size. This criterion ensures that we remove significantly extended sources while preserving compact and point-like sources.

At the SMC distance of 62.44 ± 0.47 kpc, $1'' \simeq 0.303$ pc. Thus, the ASKAP beams correspond to physical scales of $\sim 14.5'' \times 12.2'' \approx 4.39 \times 3.69$ pc at 944 MHz and $\sim 8.7'' \times 8.2'' \approx 2.63 \times 2.48$ pc at 1367 MHz. Our 1.2× beam-size threshold therefore translates to excluding sources larger than $\sim 17.4'' \times 14.6'' \approx 5.27 \times 4.43$ pc (944 MHz) and $\sim 10.44'' \times 9.84'' \approx 3.16 \times 2.98$ pc (1367 MHz).

This selection method may introduce minor biases, such as the inclusion of faint extended sources near the threshold and the exclusion of marginally resolved sources due to beam-fitting variations. Despite these factors, the 1.2 threshold effectively balances the rejection of extended sources while preserving a reliable sample of compact radio sources.

Step 4: Correcting Integrated Flux Values

Some sources exhibited integrated flux densities lower than their peak flux densities. When a source extractor provides such results, it means that the source is unresolved, and the integrated flux density

[4] https://github.com/PaulHancock/Aegean

[5] https://github.com/PaulHancock/Aegean/blob/main/doc/includes/aegean.md

should be equal to the peak flux density. To correct these values, we applied the following logical operation:

$$S_{\rm int} = \begin{cases} S_{\rm peak}, & \text{if } S_{\rm int} < S_{\rm peak}, \\ S_{\rm int}, & \text{otherwise.} \end{cases}$$

This correction ensured that all unresolved sources in the catalogue were properly characterised. The corrected catalogue is shown in Table 2, where integrated flux densities have been adjusted.

Step 5: Local RMS Ratio Masking

To minimize contamination from high-noise regions, we removed sources located in areas where the local RMS values exceeded 2.5-sigma (65 µJy) of the background RMS noise. This threshold was chosen to balance the exclusion of sources affected by elevated background noise while retaining genuine detections. By applying this criterion, we ensured the removal of point sources with unreliable flux measurements due to high local noise levels.

Step 6: Visual Inspection and Validation

Following the masking steps, the remaining sources were visually inspected to ensure the validity of the detections, similar to the methodologies employed by Joseph et al. (2019) and Cotton et al. (2024). This step helped identify and remove any remaining artifacts, including those caused by bright compact extended (BCE) sources that had been split into multiple detections.

Step 7: Merging catalogues with different frequencies

To validate the quality and reliability of our ASKAP 944 MHz and 1367 MHz catalogues of the SMC, we performed a comprehensive comparison with the MeerKAT 1283 MHz catalogue (Cotton et al. 2024) and the Milliquas catalogue (Flesch 2023). Using TOPCAT[6] (Taylor 2005), we cross-matched the sources in our ASKAP catalogues with those in the MeerKAT catalogue within a 2″ region, ensuring accurate source alignment given the known calibration issues (Cotton et al. 2024). In this merging process, we examined the positional offsets between our ASKAP catalogues and the MeerKAT catalogue to identify any offsets or variations (see Section 4.1). Additionally, we assessed the flux densities of the matched sources to verify the consistency and reliability of the measurements across different instruments and frequencies (see Section 4.2). These multi-frequency flux comparisons also enabled the estimation of spectral indices, providing insight into the emission properties of radio sources across the SMC field (see Section 4.3). To assess the reliability of the spectral index fits, we computed reduced chi-squared (χ^2_ν) values for each source (see Section A.3).

[6] http://www.starlink.ac.uk/topcat/

Step 8: Cross-matching with SIMBAD

As a final step, our catalogue was cross-matched with the SIMBAD database using the CDS X-Match service (Boch et al. 2012) within a 2″ region to identify known source types. This procedure yielded 800 matched sources. The distribution of these sources by object type is shown in Fig. 3. The dominant populations are galaxies (G; 22.6%), radio sources (Rad; 14.1%), AGN candidates (AG?; 12.1%), and confirmed AGNs (10.5%). Additional notable classes include radio galaxies (rG), radio binaries (RB?), and X-ray sources (X), each contributing between 5–6% of the total. The remaining categories are less frequent types such as PNe, candidate YSOs (Y*?), and pulsars (Psr). All remaining classifications with individual contributions below 1% are grouped under "Others" in the figure. This category includes a wide range of less common radio sources, including quasi-stellar objects (QSOs), emission-line galaxies (Em*), Seyfert galaxies (Sy1, Sy2, SyG), H II regions (H II), stellar clusters (Cl*), Supernovas (SNs), white dwarf candidates (WD?), and several classes of variable and evolved stars (e.g., LP*, RR*, dS*, and Mi*). This cross-matching step gives a valuable overview of the contents of the catalogue in terms of the different populations of the SMC, including PNe, SNRs, radio stars, and background sources. Approximately 59% of the 800 matched sources correspond to extragalactic sources located within the field of the SMC region but lying beyond the SMC itself.

4. RESULTS

Following the catalogue generation methodology outlined in Section 3, the original 944 MHz catalogue of 97,877 sources was filtered to 36,571 reliable sources distributed across the field. Most excluded sources were located at the field edges or in regions with BCE sources, as shown in Fig. 4.

The 1367 MHz catalogue was generated using the same methodology as the 944 MHz catalogue, from an initial 123,435 detected sources; this process yielded a filtered catalogue of 15,227 reliable sources.

4.1. Positional Offsets

Accurate positional measurements are critical for reliable source identification and multi-wavelength cross-matching in radio astronomy (Turtle et al. 1998). By comparing the positions of sources in our ASKAP catalogues with those in the MeerKAT 1283 MHz catalogue (Cotton et al. 2024) and the Milliquas catalogue (Flesch 2023), we assess the astrometric precision of our data. Small positional offsets ensure that our catalogues can be effectively used for astrophysical studies, improving upon the positional accuracy of earlier ASKAP surveys (Joseph et al. 2019).

The positional comparison of ASKAP 944 MHz vs. MeerKAT 1283 MHz shows mean $\Delta\mathrm{RA} = -0\farcs33$

Table 2: Example of the ASKAP 944 MHz and 1367 MHz point source catalogue of 45,886 objects in the directions of the SMC with their positions, peak and integrated flux densities. The columns provided are as follows: (1) Source name; (2 and 3) source position; (4 and 5) source peak and integrated flux density at 944 MHz with associated uncertainty; (6 and 7) source peak and integrated flux density at 1367 MHz with associated uncertainty; (8) spectral index (α) fitted using all available frequency measurements (ASKAP 944/1367 MHz and up to 12 MeerKAT sub-bands) with the associated error; (9) number of flux-density measurements used in the spectral index fit. The full catalogue is provided through the VizieR service and as supplementary material.

Name	RA (J2000)	Dec (J2000)	$S_{peak\,944\,MHz}$ (mJy beam^{-1})	$S_{int\,944\,MHz}$ (mJy)	$S_{peak\,1367\,MHz}$ (mJy beam^{-1})	$S_{int\,1367\,MHz}$ (mJy)	$\alpha \pm \Delta\alpha$	n
J003334–703819	00:33:34	–70:38:19	0.168±0.008	0.168±0.008	0.171±0.009	0.176±0.009	–0.36±0.46	7
J002906–745338	00:29:06	–74:53:38	0.537±0.027	0.537±0.027	0.420±0.021	0.420±0.021	–0.98±0.089	14
J004938–741929	00:49:38	–74:19:29	0.260±0.013	0.354±0.018	0.135±0.007	0.135±0.007	–1.68±0.31	12
J005535–722836	00:55:35	–72:28:36	0.733±0.037	0.747±0.037	0.437±0.022	0.565±0.028	–0.90±0.11	14
J005701–715359	00:57:01	–71:53:59	0.494±0.025	0.509±0.025	0.297±0.015	0.390±0.020	–0.87±0.14	14
J005833–723212	00:58:33	–72:32:12	0.617±0.031	0.617±0.031	0.683±0.034	0.733±0.037	0.17±0.08	14
J005617–704541	00:56:17	–70:45:41	0.278±0.014	0.317±0.016	0.297±0.015	0.297±0.015	–0.45±0.18	12
J011031–715711	01:10:31	–71:57:11	0.234±0.012	0.234±0.012	0.146±0.007	0.159±0.008	–0.84±0.21	12
J013559–713914	01:35:59	–71:39:14	0.339±0.017	0.339±0.017	0.206±0.010	0.212±0.011	–0.86±0.26	13
J004538–734546	00:45:38	–73:45:46	0.189±0.009	0.189±0.009	0.205±0.010	0.205±0.010	–0.30±0.22	11
J002716–695752	00:27:16	–69:57:52	0.443±0.022	0.452±0.023	0.393±0.020	0.426±0.021	–0.81±0.24	14
J013215–740949	01:32:15	–74:09:49	0.200±0.010	0.200±0.010	0.134±0.007	0.134±0.007	–0.87±0.36	12
J013629–703303	01:36:29	–70:33:03	1.093±0.055	1.138±0.057	0.644±0.032	0.756±0.038	–0.48±0.11	14
J013121–711130	01:31:21	–71:11:30	2.362±0.118	2.472±0.124	1.961±0.098	2.083±0.104	–0.41±0.049	14
J011312–711956	01:13:12	–71:19:56	0.153±0.008	0.172±0.009	0.161±0.008	0.189±0.009	–0.57±0.33	12

(STDEV = 0.77) and ΔDEC = 0.″23 (STDEV = 0.72) (see Fig. 5).

The positional comparison of ASKAP 1367 MHz vs. MeerKAT 1283 MHz shows mean ΔRA = −0.″27 (STDEV = 0.63) and ΔDEC = 0.″14 (STDEV = 0.64) (see Fig. 5).

To further assess the positional accuracy of our ASKAP catalogues, we compared them to the latest version of the Milliquas catalogue (Flesch 2023), using a 2″ crossmatching radius, consistent with the ASKAP comparison. This comparison included both the ASKAP 944 MHz and 1367 MHz catalogues, as well as the MeerKAT 1283 MHz catalogue, to determine which telescope provides better positional accuracy relative to Milliquas.

The positional comparison of ASKAP 944 MHz vs. Milliquas shows mean ΔRA = –0.″37 (STDEV = 0.67) and ΔDEC = 0.″24 (STDEV = 0.7) (see Fig. 5).

The positional comparison of ASKAP 1367 MHz vs. Milliquas shows mean ΔRA = –0.″28 (STDEV = 0.6) and ΔDEC = 0.″35 (STDEV = 0.6) (see Fig. 5).

4.2. Flux Densities Comparison

To validate the flux calibration of our catalogue, we compared integrated flux densities of ASKAP 1367 MHz with the MeerKAT 1283 MHz catalogue (Cotton et al. 2024). These two surveys have closely matched central frequencies, enabling direct and meaningful comparisons.

We matched sources between the two catalogues and examined their flux density correlations across multiple signal-to-noise (S/N) thresholds see Fig. 6). A total of 27,480, 20,524, 9,300, 4,289, and 1,777 sources were identified with detection significances above 3σ, 5σ, 10σ, 20σ, and 50σ, respectively. The flux densities of these subsets were compared using a linear regression model, yielding consistent slopes: 1.037 at 3σ, 1.048 at 5σ, and 1.050 at 50σ, indicating strong agreement across different S/N regimes (see Fig. 7).

4.3. Spectral Index

The spectral index (α) is a key diagnostic parameter in radio astronomy. We use the definition $S_\nu \propto \nu^\alpha$, where S_ν is the flux density at frequency ν. It plays a central role in classifying radio sources and identifying their dominant radiation processes (Whittam et al. 2013).

For instance, synchrotron-dominated sources such as AGN jets and SNRs typically display steep spectral indices ($\alpha < -0.3$), while thermal bremsstrahlung from HII regions tends to produce flatter or even positive spectral indices (Joseph et al. 2019). The details about spectral index calculations and fitting methods are shown in the Section A.1.

In this study, spectral indices are derived using at least three distinct frequencies across flux density measurements from ASKAP (944 MHz, 1367 MHz) and MeerKAT's L-band (14 sub-bands, with bands 8 and 9 typically flagged due to RFI) spanning 908 to 1656 MHz, enabling a robust evaluation of the astrophysical consistency and reliability of our catalogues.

In total, we obtained spectral index estimates for 21,442 sources (see Fig. 8). Among these, 16,172 sources have $\alpha < -0.3$, while 2,895 have $\alpha > -0.3$. A subset of 2,726 sources, each with flux density measurements at all 14 frequencies, $S_\nu > 1$ mJy, spectral index uncertainty $\Delta\alpha < 0.2$, and reduced chi-squared $\chi^2_\nu < 1$, was used for the detailed spectral index versus flux analysis shown in Fig. 8, as these

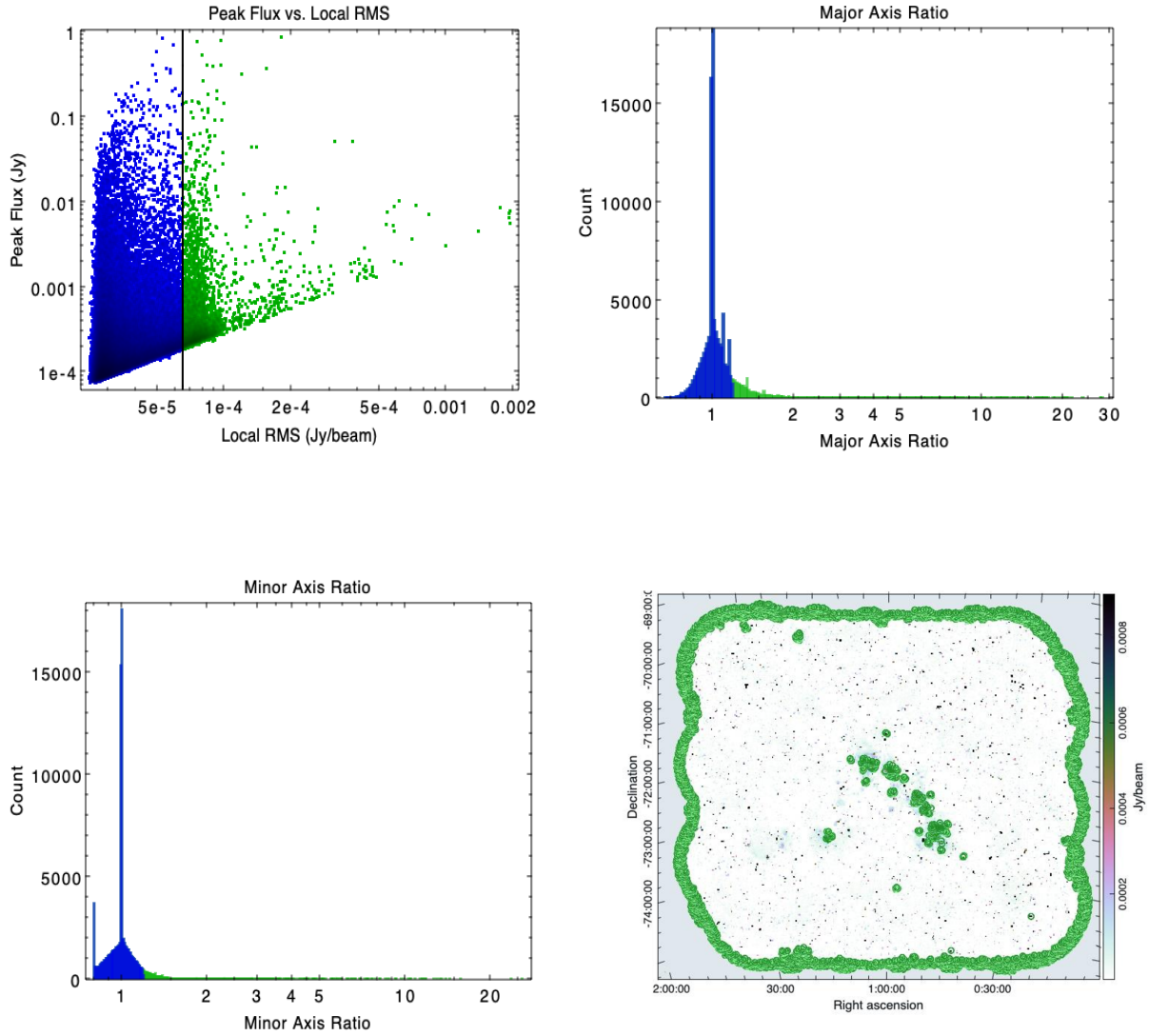

Fig. 4: Overview of ASKAP 944 MHz analysis results. **Top Left**: Peak flux as a function of RMS for ASKAP 944 MHz on a logarithmic scale. The grey line indicates the threshold at 65 μJy beam^{-1}. Retained sources are in blue and discarded sources in green. **Top Right**: Major Axis Ratio distribution for ASKAP 944 MHz sources. Retained sources are in blue, and discarded sources are in green. **Bottom Left**: Minor Axis Ratio distribution for ASKAP 944 MHz sources. Retained sources are in blue, and discarded sources are in green. **Bottom Right**: ASKAP 944 MHz image with green circles representing the masked sources, predominantly located at the edges of the image and in regions with BCE sources.

criteria ensure the robustness of the fitted spectral indices. An example of a good spectral index model fit is shown in Fig. 9.

For sources with $\chi^2_\nu < 1$, the original flux density uncertainties from the catalogue were retained (see Fig. 10). However, a significant fraction of fits showed elevated reduced χ^2_ν values, which can have numerous causes. We found that these elevated values corresponded to sources with significantly underestimated flux density uncertainties, a known issue with the Aegean program (Hancock et al. 2018). We therefore adopted a conservative error model for sources with $\chi^2_\nu \gg 1$, assuming a 5% flux density uncertainty for sources with $S_\nu > 1$ mJy and 10% for those with $S_\nu < 1$ mJy (see Fig. 11). We find that this method improves the spectral index fits and removes this fraction of elevated χ^2_ν values, indicating that the issue arose from underestimated uncertainties rather than poor model behavior. This selective adjustment provided a more realistic error estimation and improved the statistical reliability of the spectral index fit. These analyses build on previous ASKAP surveys (Joseph et al. 2019) and provide a robust foundation for studying radio source popula-

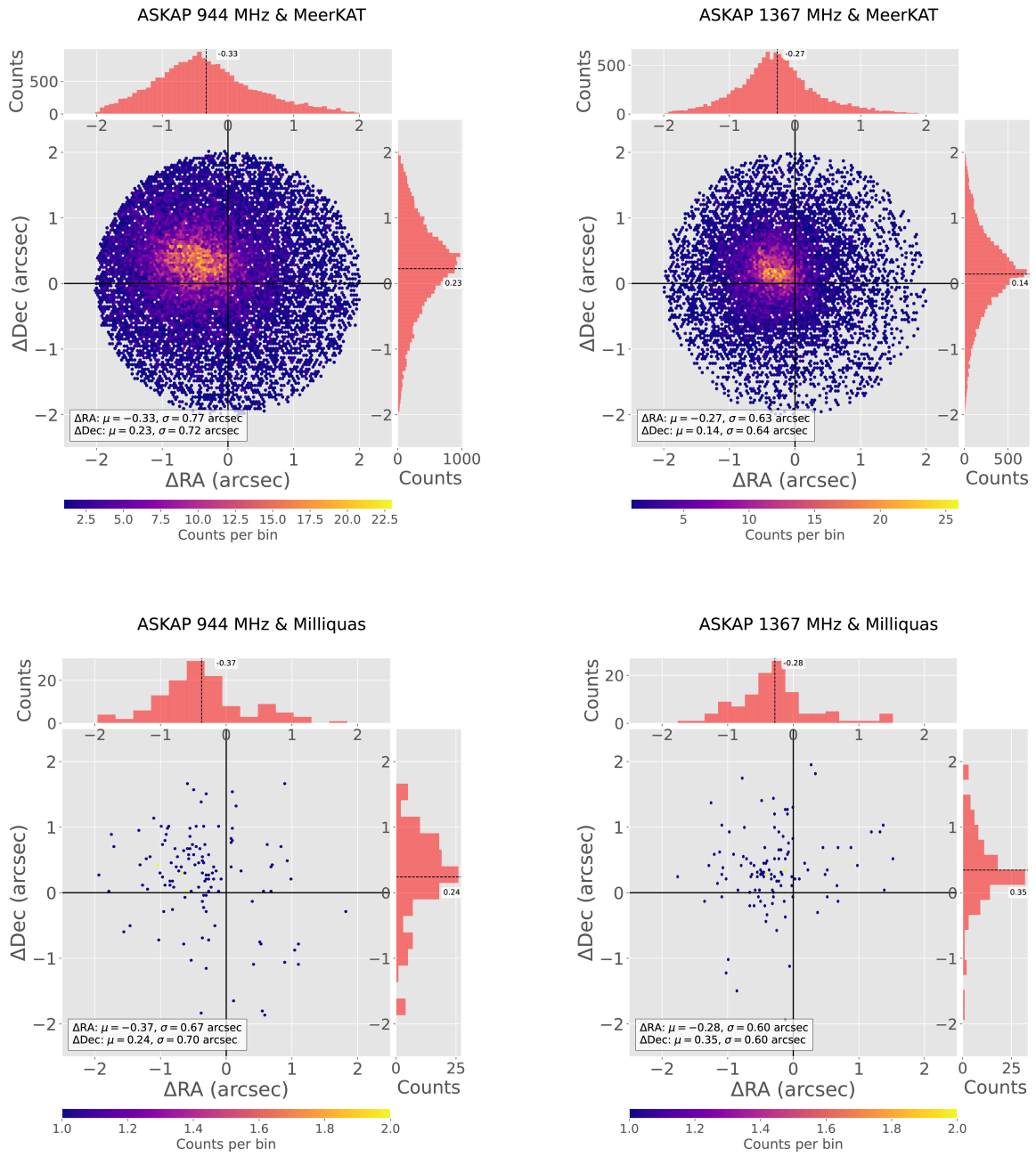

Fig. 5: Positional differences between ASKAP and external catalogues, based on cross-matching at 2″ radius. Each panel displays local density-colour-coded hexbin maps and marginal histograms. The black dashed lines in the red histograms represent the median values of the respective distributions. The points are colour-coded to indicate local density, from yellow for high density to purple for low density.

tions in the SMC, including galaxies, active galactic nuclei (AGN), and supernova remnants (SNRs). Results are presented in Section 4.

5. DISCUSSION

Compared to the earlier ASKAP-EMU observations of the SMC by Joseph et al. (2019), which reported RMS noise levels of 186 μJy beam^{-1} at 960 MHz and 165 μJy beam^{-1} at 1320 MHz, detecting 4,489 and 5,954 sources, respectively, our ASKAP surveys achieved substantially lower RMS noise levels of 26 μJy beam^{-1} at 944 MHz (see Fig. 1) and 28 μJy beam^{-1} at 1367 MHz (see Fig. 2), with significantly higher source counts of 36,571 and 15,227, respectively. These improvements highlight the enhanced imaging sensitivity and refined calibration achieved in our observations of the SMC field.

The statistical analysis of positional offsets reveals minor systematic differences between the ASKAP and MeerKAT catalogues, with mean

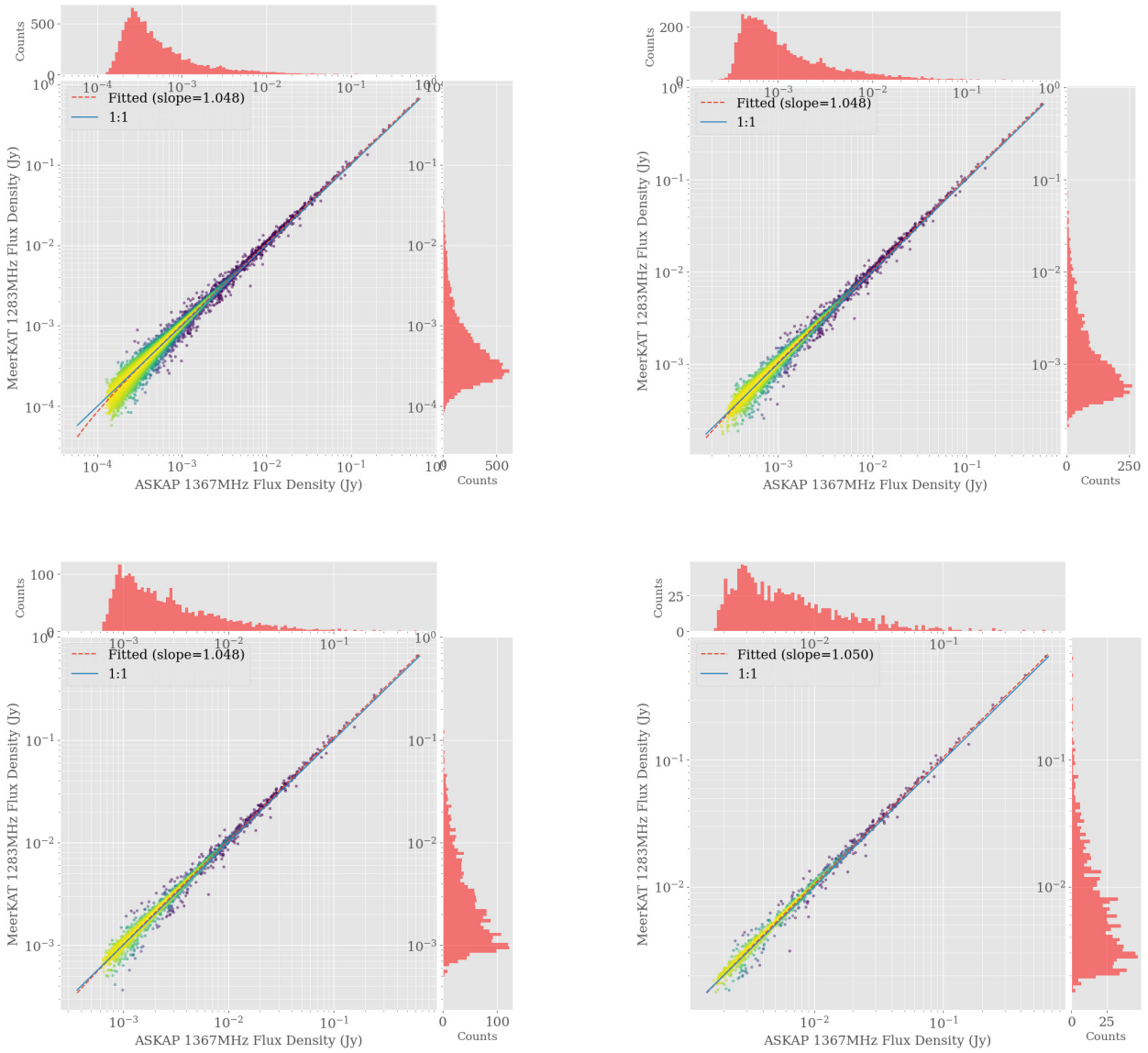

Fig. 6: Flux density comparisons between ASKAP 1367 MHz and MeerKAT 1283 MHz under varying signal-to-noise thresholds and visual encodings. The four panels correspond to catalogue matches for $\geq 5\sigma$, $\geq 10\sigma$, $\geq 20\sigma$, and $\geq 50\sigma$ sources, respectively. Sources are colour-coded by local density, with yellow indicating high density regions and purple indicating low density regions.

positional deviations remaining well within subarcsecond precision, indicative of good astrometric alignment. In contrast, Cotton et al. (2024) reported $\sim 1''$ offsets when comparing MeerKAT positions to those from the earlier ASKAP-EMU survey (Joseph et al. 2019), highlighting a clear improvement in astrometric accuracy in our current dataset. Furthermore, the comparison between ASKAP and Milliquas source positions exhibits similar consistency, supporting a typical positional uncertainty of $\sim 0\farcs3$ in our ASKAP point source catalogue.

Our flux density comparison between ASKAP 1367 MHz and MeerKAT 1283 MHz confirms a consistent linear relationship across varying S/N regimes. The fitted slope remains stable at ~ 1.05, indicating a small but consistent offset in flux scale. Marginal histograms confirm a narrowing of flux distribution at higher confidence levels, consistent with reduced noise contamination. While the results show excellent agreement for bright sources, a noticeable increase in scatter emerges at lower flux densities ($S_\nu < 1.2$ mJy), particularly at the 3σ and 5σ levels (see Fig. 7). This divergence is likely driven by differences in beam sizes, calibration uncertainties and underestimated uncertainties in faint sources.

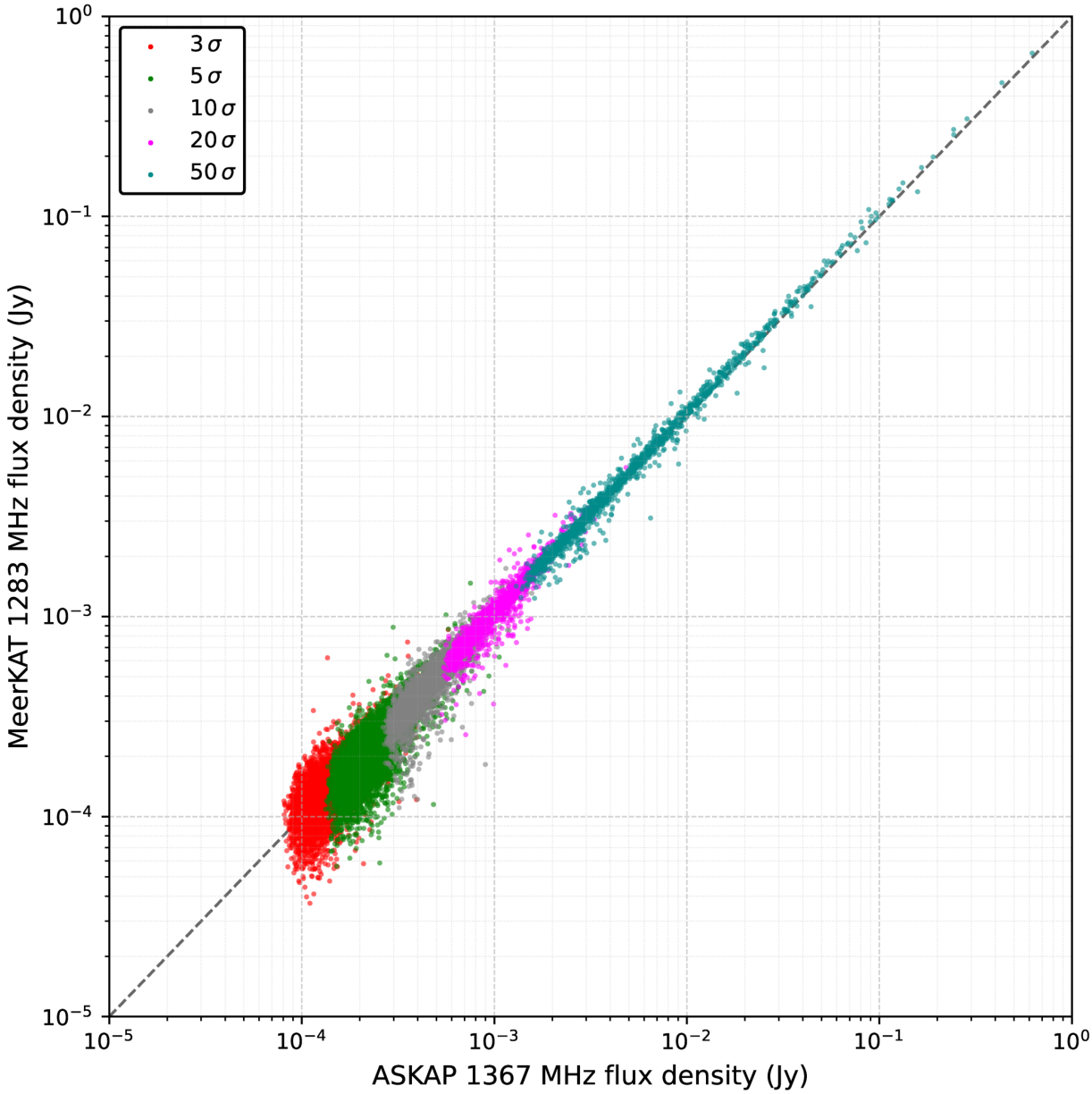

Fig. 7: Flux density comparisons between ASKAP 1367 MHz and MeerKAT 1283 MHz across all sources from 3σ to 50σ, colour-coded by signal-to-noise ratio (S/N), ranging from 3σ (red) to 50σ (cyan). The fitted slope remains consistent across S/N bins, indicating robust flux agreement.

Compared to the earlier ASKAP–MeerKAT flux comparison in Cotton et al. (2024), which found agreement only at high S/N ($>50\sigma$), our analysis reveals a tighter correlation and broader consistency across lower thresholds. This improvement reflects both deeper imaging and refined calibration in our new ASKAP dataset.

The results of our spectral index analysis show that the majority of sources in our catalogue exhibit spectral indices within the range $-1.7 < \alpha < +1.5$, in line with expectations from earlier radio continuum studies of the SMC. Previous analyses, such as Cotton et al. (2024), reported typical spectral index distributions falling within $-2.5 < \alpha < +1.5$. The distribution peaks around $\alpha \approx -0.8$, characteristic of synchrotron-dominated emission from SNRs and AGNs, while a substantial population with $\alpha > -0.3$ likely corresponds to thermal emission from HII regions and planetary nebulae.

To ensure the reliability of the spectral index measurements, we applied strict selection criteria, including detections at 14 frequency-flux measurements, uncertainties $\Delta\alpha < 0.2$, and reduced chi-squared values $\chi^2_\nu < 1$ (see Section A.3). This fil-

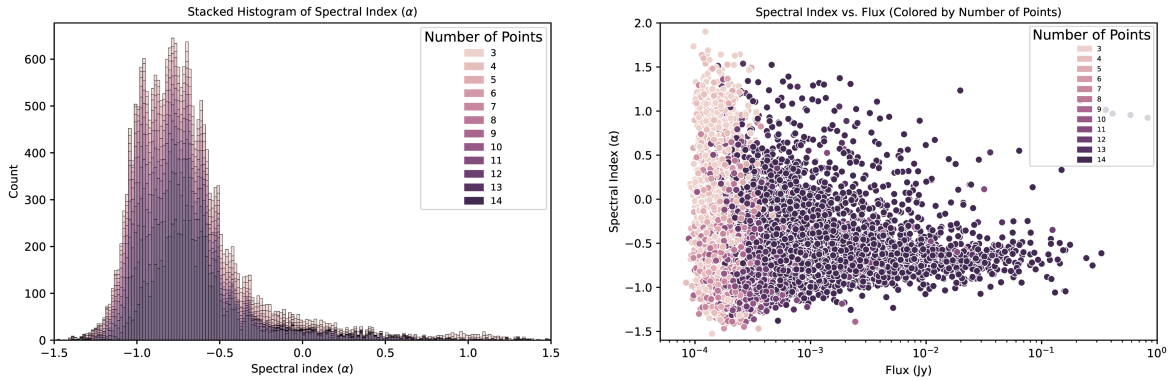

Fig. 8: Distribution of spectral indices across 14 different frequencies from ASKAP and MeerKAT. **Left**: Stacked histogram showing the point source spectral index distribution. The colours represent the number of channels used in the spectral index fit. **Right**: Scatter plot showing the distribution of spectral indices per integrated flux density. The colours represent the number of channels used in the spectral index fit. In both figures, light colours represent small numbers, and dark colours represent high.

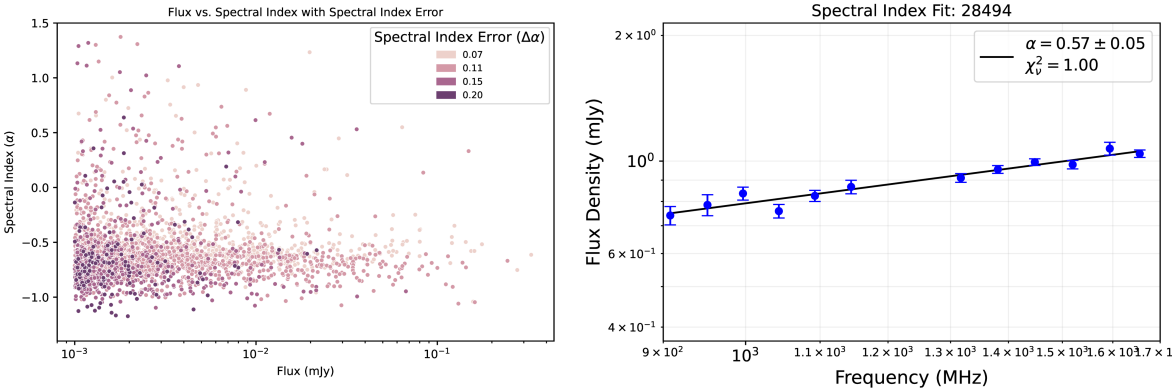

Fig. 9: **Left**: The distribution of spectral indices per integrated flux densities for 2,726 sources. The sources were restricted to those with 14 frequency-flux measurements, flux density >1 mJy, spectral index error $\Delta\alpha < 0.2$, and $\chi^2_\nu < 1$. The colour bar represents the spectral index fit error. **Right**: Example of a spectral index distribution of the source with `mainID 28494` ($\chi^2_\nu = 1$). Flux density is plotted as a function of frequency on a log–log scale. The solid black line represents the orthogonal distance regression (ODR) fit in log space, from which the spectral index (α) and reduced chi-squared (χ^2_ν) were derived. Vertical error bars indicate the assumed flux density uncertainties. All 14 available frequency measurements were used in both fits.

tering yielded 2,726 robust spectral index estimates across the SMC field.

A direct comparison with the MeerKAT results of Cotton et al. (2024) reveals excellent consistency: our mean spectral index is $\alpha = -0.62 \pm 0.35$, closely matching their reported $\alpha = -0.65 \pm 0.37$. This alignment confirms the accuracy of our ASKAP flux density measurements and underscores the coherence between the ASKAP and MeerKAT datasets.

Overall, the consistency of our spectral index measurements with previous studies highlights the reliability of our dataset and enhances the understanding of the radio-emitting population in the SMC. These results provide a strong foundation for future multi-wavelength studies of the SMC's radio sources.

5.1. Spectral index mapping for merged images

To complement our point source spectral index catalogue and provide spatial context for extended and diffuse emission, we constructed a spectral index map of the SMC region using MIRIAD[7] (Sault et al. 1995). This map was derived from the ASKAP 944 MHz and 1367 MHz images and the MeerKAT 1283 MHz image (Fig. 12), allowing pixel-wise characterization of spectral behaviour across the field.

To ensure uniform resolution and astrometric consistency, all input images were convolved to a common beam size of $20'' \times 20''$ using CONVOL, and

[7] http://www.atnf.csiro.au/computing/software/miriad/

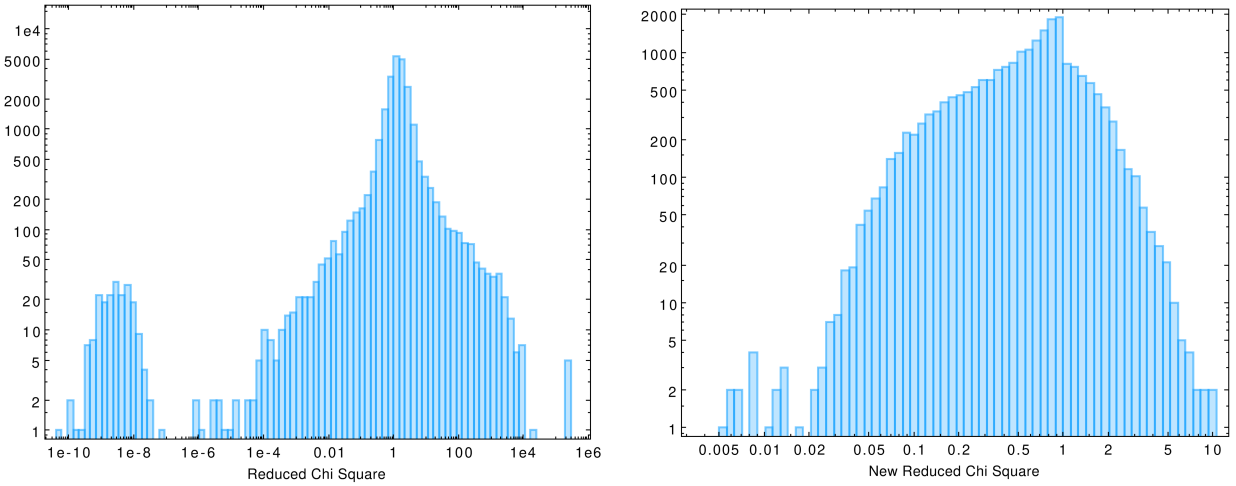

Fig. 10: **Left**: Initial distribution of reduced chi-squared (χ^2_ν) values for spectral index fits, computed using flux density uncertainties directly extracted from the catalogue. **Right**: Updated distribution of reduced chi-squared (χ^2_ν) values for the same sources, recalculated after applying uniform flux density uncertainties: ±5% for sources with $S_\nu > 1$ mJy and ±10% for sources with $S_\nu < 1$ mJy. Both distributions are shown on log–log scales to highlight the improvement in the fit quality after addressing underestimated uncertainties.

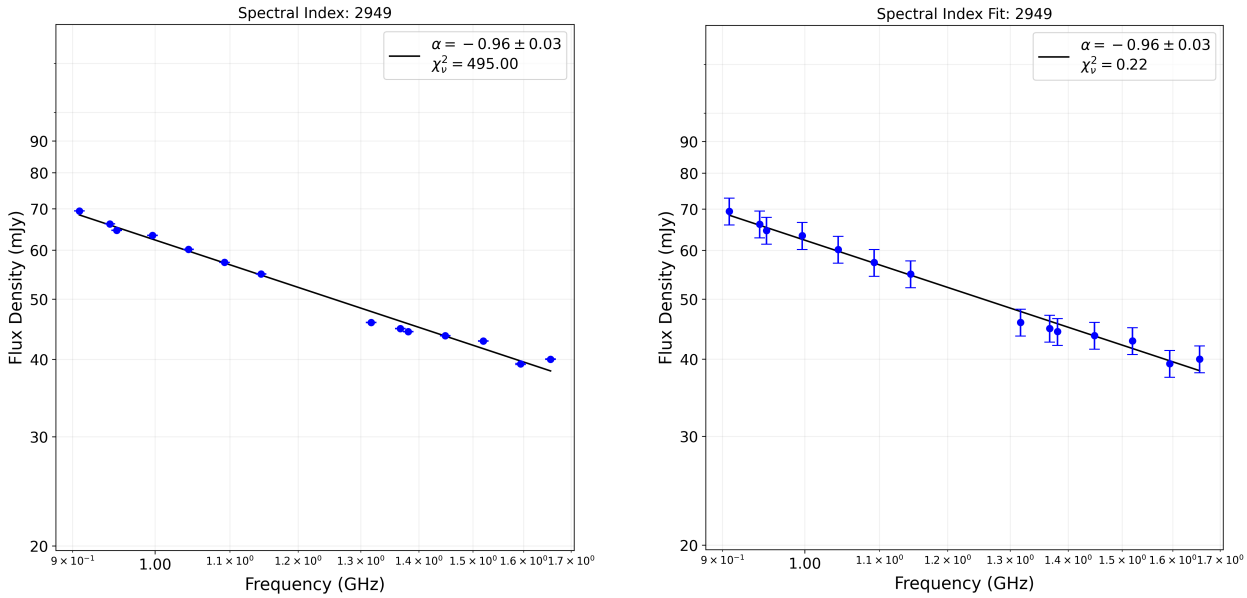

Fig. 11: **Left**: Spectral index distribution of the source with `mainID 2949` using real flux density errors from the catalogue, with reduced chi-squared $\chi^2_\nu = 495.00$. **Right**: Same source, but assuming a flat ±5% flux density error for all points, with $\chi^2_\nu = 0.22$. In both panels, flux density is plotted as a function of frequency on a log–log scale. The solid black line represents the orthogonal distance regression (ODR) fit in log space, from which the spectral index (α) and reduced chi-squared (χ^2_ν) were derived. Vertical error bars indicate the assumed flux density uncertainties. All 14 available frequency measurements were used in both fits.

regridded to a common pixel scale of $2'' \times 2''$ using REGRID. The MATHS task was then used to compute the spectral index values pixel by pixel. Although no formal uncertainty map was computed, the image was inspected to ensure that spectral indices were only evaluated in regions with significant emission above the local noise threshold at all three frequencies.

The spectral index map shows that the bulk of the emission throughout the SMC displays steep spectral indices, largely in regions of significant star-forming complexes and SNRs. While full physical interpretation is outside the scope of this paper, the spectral index map marks a valuable data image. It offers a resolved tool for future studies to categorise extended

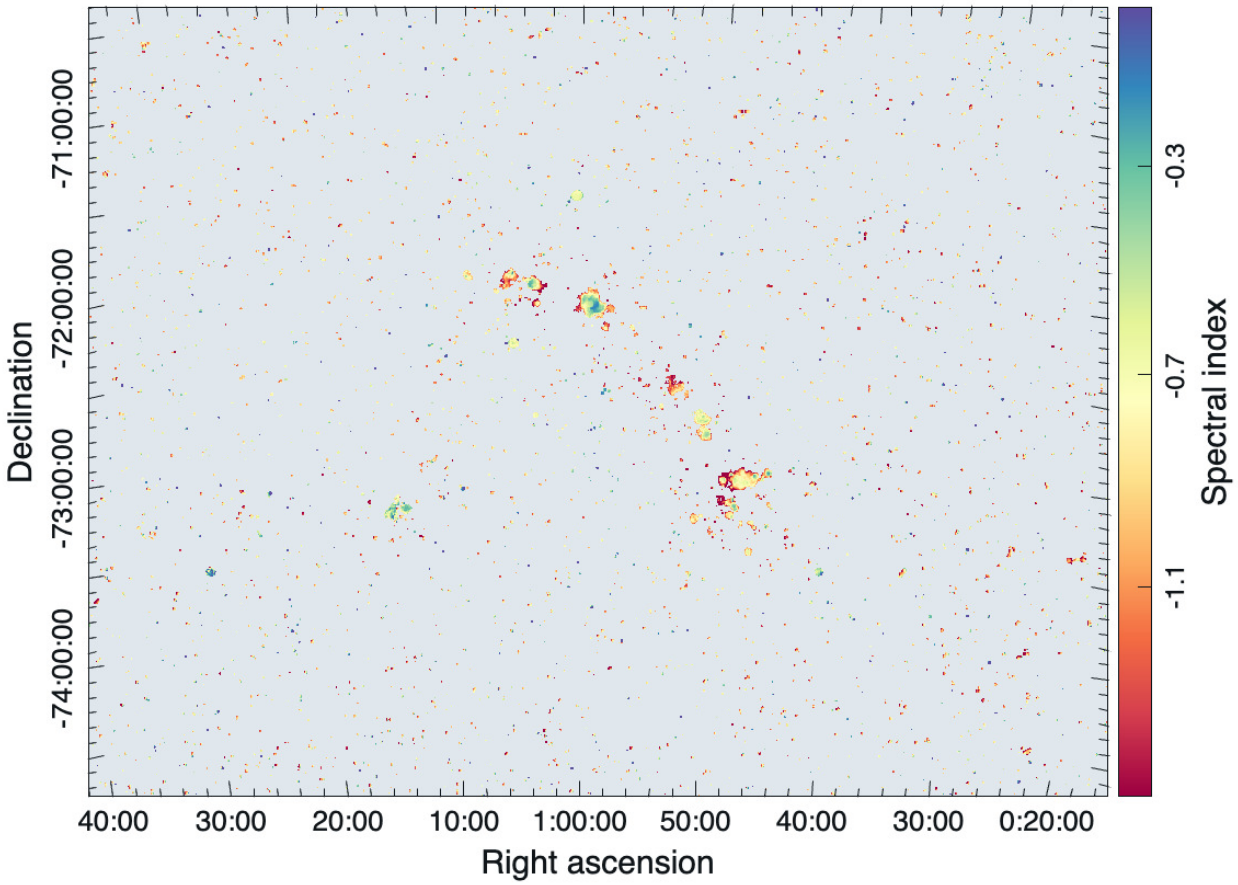

Fig. 12: Spectral index image of the SMC region using ASKAP (944 MHz and 1346 MHz) and MeerKAT (1283 MHz) images. All images have been convolved to the beam size of $20'' \times 20''$ and regridded to the largest pixel size of $2'' \times 2''$. The colour bar is linearly scaled.

sources, distinguish thermal and non-thermal emission, and explore environmental variations in the radio spectral properties of the SMC.

6. CONCLUSION

We summarise our results as follows:

- **Point source identification**: The new ASKAP surveys of the SMC field at 944 and 1367 MHz have identified a combined total of 36,571 and 15,227 point radio sources (Table 2).
- **Astrometric precision**: Positional offsets between the ASKAP and MeerKAT catalogues are within sub-arcsecond precision, with typical offsets of $\sim 0\farcs3$, indicating improved astrometric alignment relative to earlier ASKAP catalogue (Joseph et al. 2019).
- **Flux density measurements**: Flux density measurements show strong agreement between ASKAP 1367 MHz and MeerKAT 1283 MHz, with stable regression slopes near unity across a wide range of signal-to-noise thresholds. This confirms the consistency of flux calibration across instruments and detection regimes.
- **Spectral index distribution**: The spectral index distribution of sources is consistent with previous studies (Cotton et al. 2024), with a mean of $\alpha = -0.62 \pm 0.35$. The distribution peak at $\alpha \approx -0.8$ reflects a predominance of non-thermal emission sources.

Overall, these catalogues aid in advancing our understanding of the SMC population. These catalogues can be used as a foundation for future studies of the SMC and enable a better understanding of the nature of the individual sources.

DATA AVAILABILITY

Catalogs of radio continuum sources observed at 944 MHz (36,571 sources) and 1367 MHz (15,227 sources) are available in machine-readable format at `http://saj.matf.bg.ac.rs/211/ASKAP.zip`. The same catalogues will also be available via the VizieR service at CDS (`https://cds.u-strasbg.fr/`).

Acknowledgements – This scientific work uses data obtained from Inyarrimanha Ilgari Bundara / the Murchison Radio-astronomy Observatory. We acknowledge the Wajarri Yamaji People as the Traditional Owners and native title holders of the Ob-

servatory site. CSIRO's ASKAP radio telescope is part of the Australia Telescope National Facility[8]. Operation of ASKAP is funded by the Australian Government with support from the National Collaborative Research Infrastructure Strategy. ASKAP uses the resources of the Pawsey Supercomputing Research Centre. Establishment of ASKAP, Inyarrimanha Ilgari Bundara, the CSIRO Murchison Radioastronomy Observatory and the Pawsey Supercomputing Research Centre are initiatives of the Australian Government, with support from the Government of Western Australia and the Science and Industry Endowment Fund. This research made use of the cross-match service provided by CDS, Strasbourg and of the SIMBAD database, operated at CDS, Strasbourg, France.

REFERENCES

Ahmad, A., Dai, S., Lazarević, S., et al. 2025, MNRAS, 537, 2868
Asher, A. D., Filipović, M. D., Bojičić, I., et al. 2024, Ap&SS, 369, 85
Ball, B. D., Kothes, R., Rosolowsky, E., et al. 2025, ApJ, 988, 75
Bevington, P. R. 1969, Data Reduction and Error Analysis for the Physical Sciences (New York: McGraw-Hill)
Boch, T., Pineau, F., and Derriere, S. 2012, in Astronomical Society of the Pacific Conference Series, Vol. 461, Astronomical Data Analysis Software and Systems XXI, ed. P. Ballester, D. Egret, and N. P. F. Lorente, 291
Boggs, P. T. and Rogers, J. E. 1990, SIAM Journal on Scientific and Statistical Computing, 11, 873
Bradley, A., Filipović, M. D., Smeaton, Z., et al. 2025a, PASA, 42, e101
Bradley, A., Smeaton, Z., Tothill, N., et al. 2025b, PASA, 42, e032
Burger-Scheidlin, C., Brose, R., Mackey, J., et al. 2024, A&A, 684, A150
Caleb, M., Heywood, I., Rajwade, K., et al. 2022, NatAs, 6, 828
Chapman, J. M. 2015, in IAU General Assembly, Vol. 29, 2232458
Chapman, J. M., Dempsey, J., Miller, D., et al. 2017, in Astronomical Society of the Pacific Conference Series, Vol. 512, Astronomical Data Analysis Software and Systems XXV, ed. N. P. F. Lorente, K. Shortridge and R. Wayth, 73
Clarke, J. N. 1976, MNRAS, 174, 393
Cotton, W. D., Filipović, M. D., Camilo, F., et al. 2024, MNRAS, 529, 2443
Crawford, E. J., Filipovic, M. D., de Horta, A. Y., et al. 2011, SerAJ, 183, 95
Dempsey, J., McClure-Griffiths, N. M., Murray, C., et al. 2022, PASA, 39, e034
Filipović, M. D. and Tothill, N. F. H. 2021, Principles of Multimessenger Astronomy (IOP Publishing)
Filipovic, M. D., White, G. L., Jones, P. A., et al. 1996, in Astronomical Society of the Pacific Conference Series, Vol. 112, The History of the Milky Way and Its Satellite System, ed. A. Burkert, D. H. Hartmann and S. A. Majewski, 91
Filipovic, M. D., Jones, P. A., White, G. L., et al. 1997, A&AS, 121, 321
Filipovic, M. D., Haynes, R. F., White, G. L. and Jones, P. A. 1998, A&AS, 130, 421
Filipović, M. D., Bohlsen, T., Reid, W., et al. 2002, MNRAS, 335, 1085
Filipović, M. D., Payne, J. L., Reid, W., et al. 2005, MNRAS, 364, 217
Filipović, M. D., Payne, J. L., Alsaberi, R. Z. E., et al. 2022, MNRAS, 512, 265
Filipović, M. D., Dai, S., Arbutina, B., et al. 2023, AJ, 166, 149
Filipovic, M. D., Smeaton, Z. J., Kothes, R., et al. 2025, PASA, 42, 104
Flesch, E. W. 2023, The Open Journal of Astrophysics, 6, 49
For, B.-Q., Staveley-Smith, L., Hurley-Walker, N., et al. 2018, MNRAS, 480, 2743
Gaensler, B. M., Heald, G. H., McClure-Griffiths, N. M., et al. 2025, PASA, 42, e091
Green, D. A. 2011, Bulletin of the Astronomical Society of India, 39, 289
Gupta, N., Huynh, M., Norris, R. P., et al. 2022, PASA, 39, e051
Guzman, J., Whiting, M., Voronkov, M., et al. 2019, ASKAPsoft: ASKAP science data processor software, Astrophysics Source Code Library, record ascl:1912.003
Hancock, P. J., Murphy, T., Gaensler, B. M., Hopkins, A. and Curran, J. R. 2012, MNRAS, 422, 1812
Hancock, P. J., Trott, C. M. and Hurley-Walker, N. 2018, PASA, 35, e011
Hilditch, R. W., Howarth, I. D. and Harries, T. J. 2005, MNRAS, 357, 304
Hopkins, A., Kapinska, A., Marvil, J., et al. 2025, PASA, 42, e071
Hotan, A. W., Bunton, J. D., Chippendale, A. P., et al. 2021, PASA, 38, e009
Huynh, M., Dempsey, J., Whiting, M. T. and Ophel, M. 2020, in Astronomical Society of the Pacific Conference Series, Vol. 522, Astronomical Data Analysis Software and Systems XXVII, ed. P. Ballester, J. Ibsen, M. Solar and K. Shortridge, 263
Joseph, T. D., Filipović, M. D., Crawford, E. J., et al. 2019, MNRAS, 490, 1202
Khabibullin, I. I., Churazov, E. M., Bykov, A. M., Chugai, N. N. and Sunyaev, R. A. 2023, MNRAS, 521, 5536
Koribalski, B. S., Norris, R. P., Andernach, H., et al. 2021, MNRAS, 505, L11
Kothes, R., Reich, P., Foster, T. J. and Reich, W. 2017, A&A, 597, A116
Lazarević, S., Filipović, M. D., Dai, S., et al. 2024a, PASA, 41, e032

[8] (https://ror.org/05qajvd42)

Lazarević, S., Filipović, M. D., Koribalski, B. S., et al. 2024b, Research Notes of the AAS, 8, 107
Matsuura, M., Ayley, V., Chawner, H., et al. 2022, MNRAS, 513, 1154
McConnell, D., Allison, J. R., Bannister, K., et al. 2016, PASA, 33, e042
McGee, R. X., Newton, L. M. and Butler, P. W. 1976, Australian Journal of Physics, 29, 329
Murray, C. E., Hasselquist, S., Peek, J. E. G., et al. 2024, ApJ, 962, 120
Norris, R. P., Intema, H. T., Kapińska, A. D., et al. 2021, PASA, 38, e003
Norris, R. P., Collier, J. D., Crocker, R. M., et al. 2022, MNRAS, 513, 1300
Payne, J. L., Filipović, M. D., Reid, W., et al. 2004, MNRAS, 355, 44
Payne, J. L., White, G. L., Filipović, M. D. and Pannuti, T. G. 2007, MNRAS, 376, 1793
Pingel, N. M., Dempsey, J., McClure-Griffiths, N. M., et al. 2022, PASA, 39, e005
Reid, W. A., Payne, J. L., Filipović, M. D., et al. 2006, MNRAS, 367, 1379
Sasaki, M., Zangrandi, F., Filipović, M., et al. 2025, A&A, 693, L15
Sault, R. J., Teuben, P. J. and Wright, M. C. H. 1995, in Astronomical Society of the Pacific Conference Series, Vol. 77, Astronomical Data Analysis Software and Systems IV, ed. R. A. Shaw, H. E. Payne and J. J. E. Hayes, 433
Smeaton, Z. J., Filipović, M. D., Koribalski, B. S., et al. 2024a, Research Notes of the AAS, 8, 158
Smeaton, Z. J., Filipović, M. D., Lazarević, S., et al. 2024b, MNRAS, 534, 2918
Smeaton, Z. J., Filipović, M. D., Alsaberi, R. Z. E., et al. 2025, eprint arXiv:2506.15067
Taylor, M. B. 2005, in Astronomical Society of the Pacific Conference Series, Vol. 347, Astronomical Data Analysis Software and Systems XIV, ed. P. Shopbell, M. Britton, and R. Ebert, 29
Turtle, A. J., Ye, T., Amy, S. W. and Nicholls, J. 1998, PASA, 15, 280
Urquhart, J. S., Wells, M. R. A., Pillai, T., et al. 2022, MNRAS, 510, 3389
Velović, V., Filipović, M. D., Barnes, L., et al. 2022, MNRAS, 516, 1865
Virtanen, P., Gommers, R., Oliphant, T. E., et al. 2020, Nature Methods, 17, 261
Whittam, I. H., Riley, J. M., Green, D. A., et al. 2013, MNRAS, 429, 2080
Wong, G. F., Filipovic, M. D., Crawford, E. J., et al. 2011a, SerAJ, 182, 43
Wong, G. F., Filipovic, M. D., Crawford, E. J., et al. 2011b, SerAJ, 183, 103
Wong, G. F., Crawford, E. J., Filipovic, M. D., et al. 2012a, SerAJ, 184, 93
Wong, G. F., Filipovic, M. D., Crawford, E. J., et al. 2012b, SerAJ, 185, 53
Wright, A. and Otrupcek, R. 1990, PKS Catalog (1990)

A. Appendix

A.1. Fitting Method: Orthogonal Distance Regression (ODR)

To determine the spectral index, we performed a power-law fit using Orthogonal Distance Regression (ODR), which accounts for uncertainties in both flux density and frequency measurements. ODR is preferred over ordinary least squares (OLS) regression as it minimises perpendicular residuals rather than vertical ones, making it well-suited for cases where both variables have associated errors (Boggs and Rogers 1990).

The spectral index was derived by fitting a power-law function:

$$S_\nu = B_0 \nu^\alpha, \tag{1}$$

where B_0 is the normalisation factor (flux density at a reference frequency), and α is the spectral index.

To linearise the fitting process, we rewrite this equation in logarithmic form:

$$\log S_\nu = \log B_0 + \alpha \log \nu. \tag{2}$$

This transformation allows for a linear regression approach while maintaining the power-law dependence.

We chose to use a simple power-law model (linear in log-log space) rather than higher-order polynomial fits. One of the primary reasons for this choice is to maintain consistency with MeerKAT surveys, which use the same power-law fitting method for spectral index estimation. Using the same approach ensures a direct and fair comparison between ASKAP and MeerKAT data without introducing methodological biases. Additionally, given the typical spectral behaviour of synchrotron-emitting sources, a single power-law is sufficient for most cases and avoids overfitting the data.

A.2. Implementation of the ODR Fit

Flux densities and uncertainties were extracted from the catalogue for each available frequency, and an ODR power-law model was applied using the Python library SCIPY[9] (Virtanen et al. 2020).

The fitting process was implemented as follows:

1. A power-law model was defined:

$$f(\nu) = B_0 \nu^\alpha, \tag{3}$$

where $f(\nu)$ represents the modelled flux density as a function of frequency ν, B_0 is the normalisation constant corresponding to the flux density at a reference frequency, and α is the spectral index. This function serves as the mathematical model that approximates the observed flux densities S_ν.

[9] Scipy ODR Documentation

2. ODR fitting was performed using scipy.odr.ODR:

$$\alpha = \text{ODR fit slope}, \quad B_0 = \text{ODR fit intercept}\,. \tag{4}$$

3. The best-fit parameters (α, B_0) and uncertainties were extracted.

A.3. Assessment of Fit Quality

To ensure reliability, we evaluated the fit quality using the reduced chi-squared statistic:

$$\chi^2_\nu = \frac{1}{N-p} \sum \frac{(S_{\nu,\text{obs}} - S_{\nu,\text{model}})^2}{\sigma^2}, \tag{5}$$

where, N is the number of flux density measurements for a given source, p is the number of free parameters in the model (here, $p = 2$ for α and B_0), $S_{\nu,\text{obs}}$ is the observed flux density, $S_{\nu,\text{model}}$ is the flux density predicted by the power-law fit and σ is the flux density uncertainty(Bevington 1969).

The distribution of reduced chi-squared values (χ^2_ν) for all fitted sources is shown in Fig. 10.

To exclude poorly constrained fits, we applied the following selection criteria:

- Only sources with flux density measurements at all 14 available frequencies were included.
- Only sources with flux density greater than 1 mJy were considered.
- Spectral indices with uncertainty $\Delta\alpha < 0.2$ were considered reliable.
- Sources with reduced chi-squared $\chi^2_\nu < 1$ were selected to ensure a good fit.

The final selection of sources after applying these quality filters is visualised in the left panel of Fig. 9. This scatter plot shows the distribution of spectral indices as a function of integrated flux density. The data points are colour-coded based on their spectral index uncertainty $(\Delta\alpha)$, illustrating the level of fit reliability across different flux levels. The selection criteria ensure that the retained sources have well-constrained spectral indices and statistically significant fits.

НОВА АСКАП РАДИО-КОНТИНУУМ ИСТРАЖИВАЊА МАЛОГ МАГЕЛАНОВОГ ОБЛАКА (MMO)

O. K. Khattab[1], **М. Д. Филиповић**[1], **Z. J. Smeaton**[1], **R. Z. E. Alsaberi**[2,1], **E. J. Crawford**[1], **D. Leahy**[3], **S. Dai**[4,1] **and N. Rajabpour**[1]

[1] *Western Sydney University, Locked Bag 1797, Penrith South DC, NSW 2751, Australia*
E–mail: *22197951@student.westernsydney.edu.au*

[2] *Faculty of Engineering, Gifu University, 1-1 Yanagido, Gifu 501-1193, Japan*

[3] *Department of Physics and Astronomy, University of Calgary, Calgary, Alberta, T2N IN4, Canada*

[4] *Australian Telescope National Facility, CSIRO, Space and Astronomy, P.O. Box 76, Epping, NSW 1710, Australia*

УДК 524.722.7
Оригинални научни рад

Представљамо два нова радио-континуум прегледа у оквиру ASKAP POSSUM истраживања у правцу Малог Магелановог Облака (MMO). Нове две листе радио извора које су произведене из ових прегледа садрже 36,571 радио-континуум извора посматраних на 944 MHz и 15,227 извора на 1367 MHz, са величинама снопа од $14\farcs5\times12\farcs2$ и $8\farcs7\times8\farcs2$. За креирање ових каталога тачкастих извора користили смо софтвер Aegean, а заједно са претходно објављеним MeerKAT каталогом тачкастих извора, проценили смо спектралне индексе за целу популацију заједничких радио тачкастих извора. Упоређивањем наших ASKAP каталога са MeerKAT каталогом, нашли смо 21,442 и 12,654 тачкастих радио извора заједничких за прегледе на 944 MHz и 1367 MHz а у оквиру $2''$ толеранције. Овај каталог тачкастих радио извора са радио телескопа нове генерације као што су ASKAP, помоћиће да боље изучимо различите популације радио извора.